Nano Research

Open Access

Research Article

Generation of ultrathin two-dimensional MOF-derived nanocomposites based on ion-exchange strategy with enhanced microwave absorption properties

Zuolong Ning[1,2], Hexia Huang[1]✉, Yanru He[3]✉, Yijie Liu[2], Jiaqi Tao[2], Lvtong Duan[2], Yucheng Wang[2], Zhenyu Cheng[2], Zhenglin Liu[2], and Jintang Zhou[2]

[1] College of Energy and Power Engineering, Nanjing University of Aeronautics and Astronautics, Nanjing 210016, China
[2] College of Materials Science and Technology, Nanjing University of Aeronautics and Astronautics, Nanjing 211100, China
[3] Southwest Technology and Engineering Research Institute, Chongqing 400039, China

Cite this article: *Nano Research*, **2025**, *18*, 94907283. https://doi.org/10.26599/NR.2025.94907283

ABSTRACT: Metal-organic frameworks (MOFs) materials exhibit inherent advantages in microwave absorption (MA) due to their unique compositional and structural characteristics. However, it remains a significant challenge to systematically elucidate the coordinated effects of component modulation and morphology design on electromagnetic parameters during the complex modification process to enhance the MA performance of MOFs. In this study, the two-dimensional (2D) Co-based MOFs material, layered zeolitic imidazolate framework (ZIF-L), was meticulously selected as a structure design template and combined with an efficient ion-exchange component modulation method, aiming to stimulate the potential advantages between the two in the synergistic modulation of electromagnetic parameters. Specifically, the ion-exchange method enhanced various polarization mechanisms, including interface, dipole, and defect-induced polarizations. Meanwhile, the 2D template facilitates the formation of a robust conductive network on the surface and ensures the high efficiency and uniformity of the ion-exchange process. Ultimately, the resulting material achieved an adequate absorption bandwidth (EAB) of 6.47 GHz at a thickness of 2 mm, a 78% improvement over the untreated sample (EAB = 3.64 GHz). This research not only provides valuable theoretical insights into the application of 2D MOFs materials in MA but also offers innovative perspectives for the design and development of energy-saving and environmentally friendly microwave absorption materials (MAMs).

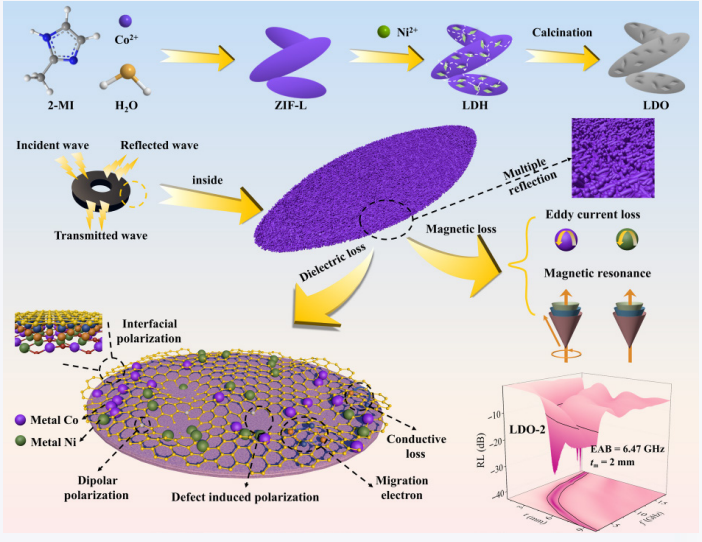

KEYWORDS: metal-organic framework, blade-like layered zeolitic imidazolate framework (ZIF-L), microwave absorption

1 Introduction

Addressing the escalating challenge of electromagnetic wave (EMW) pollution, the urgent need for efficient microwave absorption materials (MAMs) has become evident [1–3]. Metal-organic frameworks (MOFs) materials hold significant potential for microwave absorption (MA) applications due to their unique topologies, adjustable chemical compositions, and highly ordered pore structures [4, 5]. Nonetheless, pure MOFs are hampered by inherent deficiencies such as low intrinsic electronic conductivity and inadequate dielectric responses, which severely restrict their utility in MA mechanisms [6]. To surmount these obstacles, theoretical possibilities exist to achieve multifaceted functional mappings from micro to macro scales through the meticulous design of MOFs components and structures [7]. However,

Received: November 13, 2024; **Revised:** January 21, 2025
Accepted: January 27, 2025

✉Address correspondence to Hexia Huang, huanghexia@nuaa.edu.cn; Yanru He, 837377943@qq.com

unraveling the intricate interactions between component modulation and morphology design within complex modification processes and comprehending how these multifaceted elements synergistically influence electromagnetic parameters remains a formidable challenge [8–10].

In the realm of component modulation engineering for MOFs materials, the ion-exchange strategy predicated on proton shear has emerged as an efficacious method [11, 12]. This approach facilitates the heterogeneous distribution of metal elements across the MOFs surface, thereby engendering a novel metal heterogeneous phase. This heterogeneity disrupts the surface charge distribution and stimulates the migration of surface carriers. Additionally, the formation of heterogeneous interfaces during this process influences electronic spin states and the relaxation polarization process [13, 14]. Furthermore, the surface reconstruction affects the chemical bonding sites in the precursors, and pyrolysis introduces abundant polarization sites and defects [15]. In ion-exchange studies, Tao [11] and Zhang [12] separately validated the efficacy of Ni^{2+} and Al^{3+} based on ion-exchange strategies in enhancing the MA performance of the three-dimensional (3D) MOFs template zeolitic imidazolate framework (ZIF)-67. Nonetheless, existing studies have mainly focused on the advantages of ion exchange strategies in component modulation without exploring in depth the potential complementary advantages of component modulation and morphology design in modulating electromagnetic parameters.

Extensive research has demonstrated that two-dimensional (2D) materials exhibit distinct advantages in MA compared to their 3D counterparts [16, 17]. By exploiting the property of weak interlayer interference in 2D materials that facilitates modulation in the vertical direction, Yang [18] designed the 2D graphene film as a multilayer structure with optimized impedance matching and enhanced electromagnetic attenuation properties. This weak interlayer interference minimizes interfacial interference, thereby allowing precise modulation of electromagnetic parameters at the microscopic level and enabling practical macroscopic MA functionality. In the study on the application of 2D layered zeolitic imidazolate framework (ZIF-L) in MA, He [19] found that diffusion hindrance was weak at the level of the 2D material, which helped to construct an efficient surface conductive network. Additionally, the high specific surface area of 2D materials promoted the exposure of reactive oxygen vacancies, thereby increasing relaxation losses. It is due to these excellent properties that 2D materials have a promising future in the field of MA and are expected to realize the potential advantages of component modulation and morphology design in synergistically modulating electromagnetic parameters.

Considering the insights from the above discussion, this study successfully fabricated CoNi-graphite hollow porous composites through a straightforward and safe ion-exchange method, utilizing a 2D Co-based MOFs template, ZIF-L, as the research subject. Notably, Ni^{2+} was selected as a hydrolyzing agent due to its relatively weak proton cleavage force, enhancing the controllability of the ion exchange process. The transformation of the 2D template into a hollow layered double hydroxide (LDH) with a porous surface was achieved by meticulously adjusting the Ni^{2+} concentration. The ion-exchange strategy introduced abundant heterogeneous interfaces, dipoles, and defects, disrupting the original charge balance of the material and activating a multiple polarization effect. Furthermore, the unique 2D template structure created a robust conductive network due to its low diffusion energy barrier and superior electron mobility, facilitating efficient transmission and dissipation of EMW. Consequently, the CoNi-LDH-derived material demonstrated remarkable EAB (6.47 GHz) and maximum reflection loss (RL = −40.8 dB) at a matching thickness of 2 mm.

2 Experiment

2.1 Materials

Cobalt nitrate hexahydrate ($Co(NO_3)_2·6H_2O$), dimethylimidazole ($C_4H_6N_2$), methanol (MeOH), ethanol (CH_3CH_2OH), and nickel nitrate hexahydrate ($Ni(NO_3)_2·6H_2O$) were purchased from Nanjing Jingle Chemicals Co. China.

2.2 Synthesis of two-dimensional blade-like ZIF-L

100 mL of deionized water dissolved with 1.2 g of $Co(NO_3)_2·6H_2O$ was injected into 100 mL of deionized water dissolved with 2.6 g of $C_4H_6N_2$, stirred for 10 min at room temperature, and left for 4 h. After repeated washing with water, it was dried and placed in an oven at 60 °C overnight to obtain ZIF-L purple powder.

2.3 Synthesis of CoNi-LDH

0, 0.2, 0.4 and 0.6 g of $Ni(NO_3)_2·6H_2O$ were dispersed ultrasonically into 50 mL of CH_3CH_2OH. Subsequently, 0.5 g of ZIF-L was added to each of them. They were stirred at room temperature for two hours and centrifuged three times with CH_3CH_2OH. The CoNi-LDH powders were then placed and dried in an oven at 60 °C overnight. The four samples were named LDH-0, LDH-1, LDH-2, and LDH-3, corresponding to the etching concentrations from low to high.

2.4 Synthesis of CoNi@C-LDO

The prepared LDH can be transformed into layered double oxides (LDO) in the subsequent annealing process performed under nitrogen environments. The resulting powders were respectively placed in a porcelain boat. N_2 inert gas was passed into the tube furnace to protect against oxidation. The sample was heated to 300 °C and kept warm for 0.5 h. After that, the sample was heated to 700 °C from 300 °C and held for two hours. The CoNi@C blade-like MAMs were prepared using the carbothermal reduction method. The calcined product CoNi@C powder particles were collected and named as LDO-0, LD0-1, LDO-2, and LDO-3 corresponding to LDH-0, LDH-1, LDH-2, and LDH-3.

3 Results and discussion

3.1 Synthesis mechanism

Figure 1(a) demonstrates a typical ZIF-L synthesis process, the self-templated conversion to LDH by Ni^{2+} doping, and their calcination treatment to obtain derived LDO. Divalent Co ions and $C_4H_6N_2$ organic ligands were coordinated in aqueous solvents to obtain 2D blade-like ZIL-L [20]. After the introduction of Ni ions, their hydrolysis in ethanol solution produced free protons, which disrupted the coordination bonds between the clusters of ZIL-L ions and led to the formation of lamellar LDH on the blade-like surfaces by the coprecipitation of metal Co ions and hydroxide groups. During the growth of LDH, the unique 2D blade-like structure promoted and stabilized the total growth of its lamellar structure during the LDH growth process. While the low intrinsic

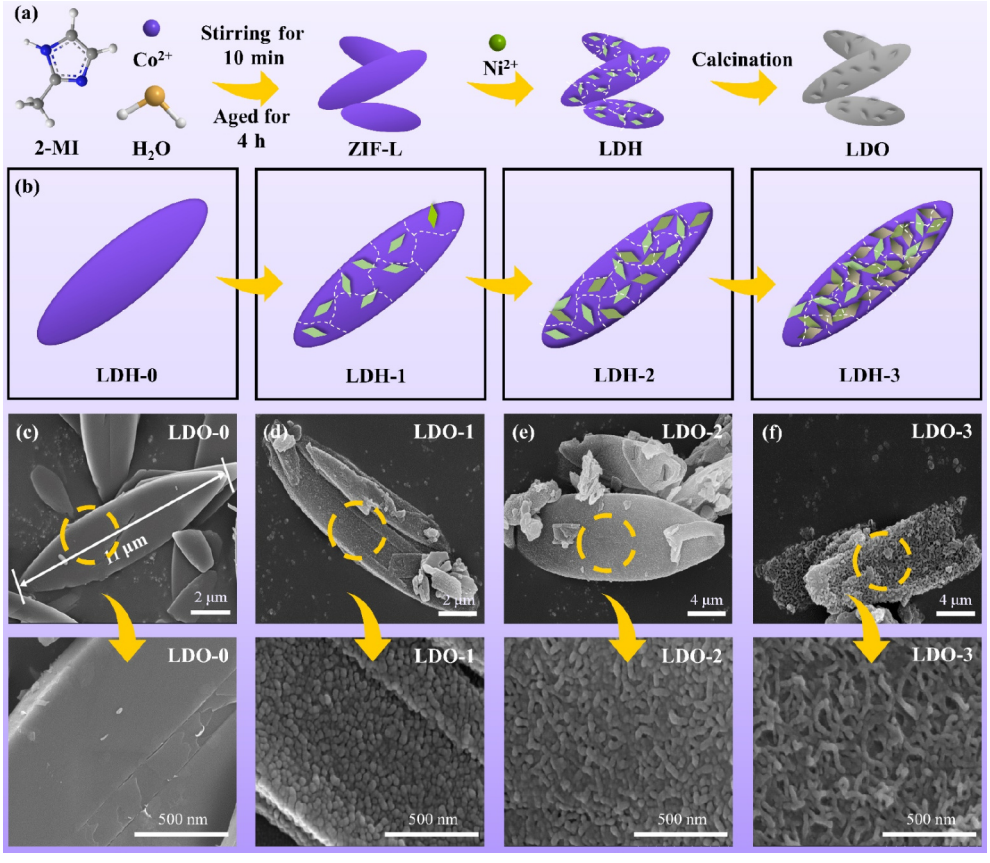

Figure 1 (a) and (b) The preparation mechanism and (c)–(f) SEM images of the samples.

conductivity of MOFs and LDH is not favorable for direct use in MA, calcined carbonization to obtain the derived LDO can significantly increase MA performance. At the same time, the doping etching effect is regulated by modulating the concentration of Ni^{2+} to explore the optimal etching concentration to match the dielectric and magnetic loss.

Figure 1(b) demonstrates the differences in the LDH obtained by ZIF-L conversion with increasing Ni^{2+} etching concentration. As shown in Fig. 1(c), the unetched ZIF-L had a nearly symmetric 2D elongated blade-like structure with a length of about 11 μm, and its surface was smooth and flat. In contrast, in Fig. 1(d), a slight disintegration of the blade-like structure occurred, and shorter LDH particles were formed on the surface after etching at low concentrations. However, its surface remains relatively smooth. At this time, the conversion of ZIF-L to LDH was incomplete, and ZIF-L coexisted with LDH. As shown in Fig. 1(e), the original blade-like structure of ZIF-L further disintegrated under the etching of medium concentration conditions. However, it remained relatively intact and formed abundant and dense CoNi-LDH nanotubes on the surface. The surface was rougher relative to the low-concentration etch product. With further increase in the etching concentration, the blade-like structure of ZIF-L was very much disrupted due to Ni^{2+} induced proton attack. As shown in Fig. 1(f), the regular blade structure has nearly disappeared. Instead, the worm-type LDH forms a dense network structure with a rough and highly porous surface.

3.2 Microcosmic characterization and analysis

Figure 2 shows the scanning electron microscopy (SEM) and transmission electron microscopy (TEM) images of different precursors after calcination to obtain the product LDO and the corresponding representations. Accompanied by the increase of etching concentration, the CoNi-LDH nanosheets gradually ruptured and porous the lamellar blade structure from partially growing over the blade surface to completely eroding the encapsulated ZIF-L residue; it affected the structure of its calcined derived products LDO. From Fig. 2(a), it is not difficult to see that the uniformly distributed CoNi@C organization gradually replaced the original smooth blade-like structure with further increased etching concentration, and the thickness of the LDH derivatives increased. Among them, LDH 0-2, which maintained a blade-like structure, retains a regular 2D layered structure after calcination. LDH-3, however, ruptured further after calcination and had a somewhat irregular structure. The TEM images show the LDO carbon matrix distributed with inhomogeneous nanoparticles, shown in Fig. 2(b). Compared to LDO-0, LDO-1–LDO-3 all exhibited the hollow phenomenon, enlarging the specific surface area of the structure. This facilitated enhanced scattering and increased surface polarization, contributing to the MA properties.

In Fig. 2(c), LDO-0 was observed to have a lattice stripe of 0.345 nm, correlating to the (002) crystallographic face of C. The lattice stripe spacing corresponding to the (111) crystalline surface of fcc Co was 0.208 nm [21]. As the etching concentration increased, the two adjacent lens stripe gaps were 0.20, 0.17, and 0.12 nm better correspondence to the (111), (200), and (220) crystal planes of the CoNi alloy [22]. The diffraction concentric rings of the selected area electron diffraction (SAED) pattern correspond to the diffraction patterns of (111), (200), and (220) in Fig. 2(d).

The elemental distribution of the products can be verified from

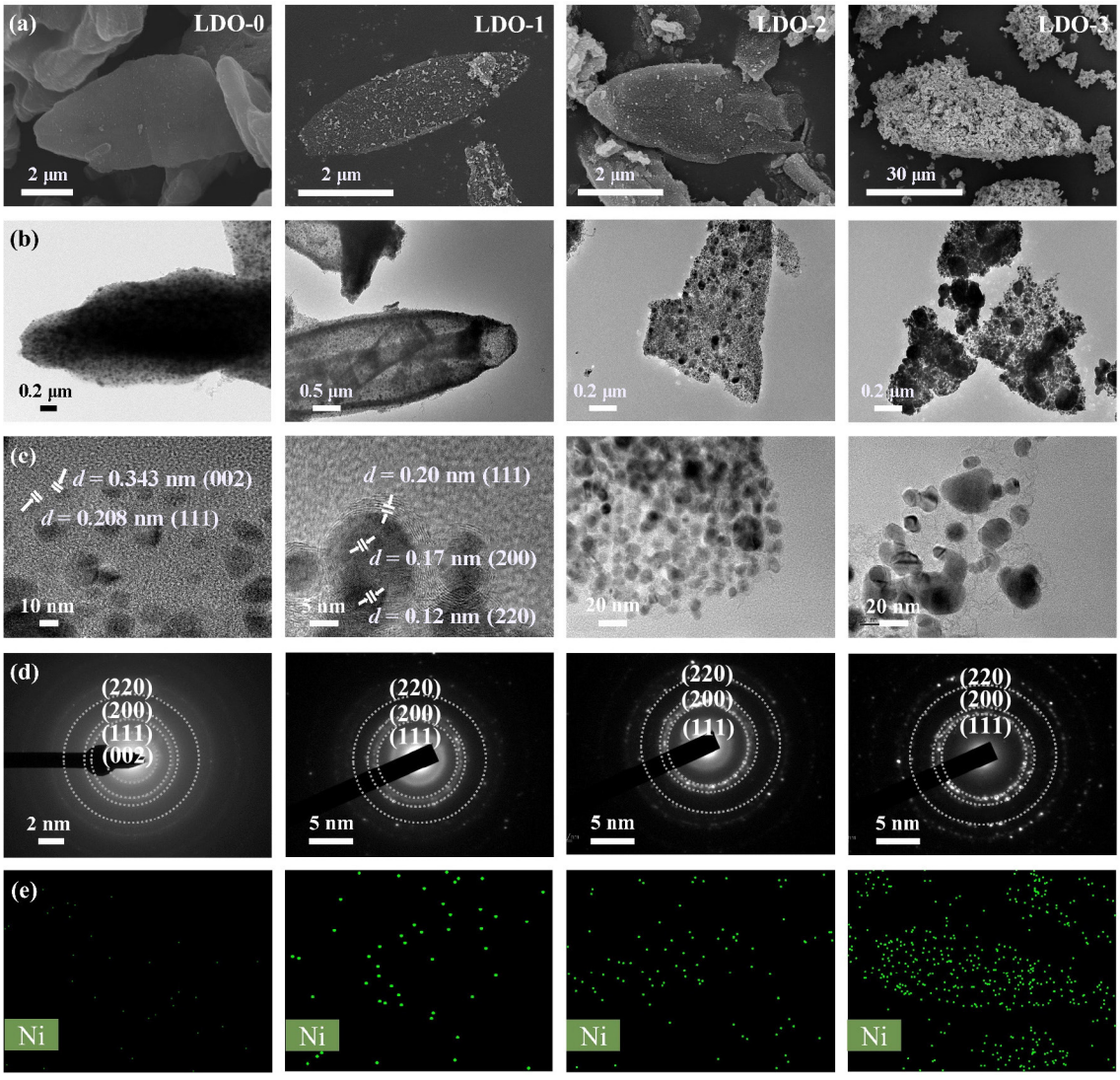

Figure 2 (a) and (b) SEM/TEM images, (c) high-resolution TEM images, (d) SAED, and (e) EDS mappings of Ni of the samples. The first to fourth columns correspond to LDO-0, LDO-1, LDO-2, and LDO-3.

the elemental mapping images in Fig. 2(e). Except for sample LDO-0, to which Ni^{2+} was not added, the presence of Ni elements was observed in all three groups of samples, verifying the successful etching of Ni^{2+}. Ni elemental content increased significantly as the etching concentration grew, verifying that etching with different concentrations of Ni^{2+} changed the Ni elemental content in the product. From the trend of Ni elemental content, the increment of LDO-1 and LDO-2 is relatively tiny. In contrast, the Ni elemental content of LDO-3 increased sharply, which is manifested as the overgrowth of CoNi-LDH, which cannot be reduced entirely to CoNi with limited carbon content, which was not conducive to the enhancement of the electrical conductivity and magnetism. The overgrowth of CoNi-LDH led to the apparent phenomenon of accumulation and the ZIF-L original 2D blade-like structure was complex to maintain, thus losing the advantage of electromagnetic loss brought by the sizeable specific surface area structure of the precursor.

Figure 3(a) demonstrates the Raman spectra of LDO. The D peak located at 1340 cm^{-1} was caused by defective carbon and atomic defects, while the in-plane stretching vibration of sp^2 hybridized carbon caused the G peak at 1581 cm^{-1} [23]. The calculated I_D/I_G [24] values (degree of graphitization) of the four groups of samples are 1.08 (LDO-0), 1.06 (LDO-1), 0.97 (LDO-2), and 1.04 (LDO-3). With the increase of the etching concentration, the I_D/I_G value showed that they decreased and then increased, and the conductive properties improved and then deteriorated as a result. The sudden increase in the I_D/I_G value of the LDO-3 sample may be the introduction of excess oxygen during the conversion of ZIF-L to CoNi-LDH. It inhibited the reduction of organic ligands to graphitized carbon during pyrolysis, increasing the degree of disorder. Figure 3(b) demonstrates the X-ray diffraction (XRD) patterns of LDO, which for LDO-0 corresponds to three peaks of Co at 44.2°, 51.5°, and 75.9°, and the (002) crystallographic plane of C at 26.1° [25]. The CoNi alloy diffraction peaks got sharper with the increase of etching concentration. In contrast, the C peaks diminished, and the diffraction peaks of CoNi alloy were gradually shifted to the side of a larger angle, all corresponding to the growing content of Ni elements.

In the electron paramagnetic resonance (EPR) spectrum of the sample (Fig. 3(c)), a Lorentzian line broadening to 3515 G (g = 2.003) was observed, which can be attributed to an oxygen vacancy defect within the material. Higher peak intensities indicate higher

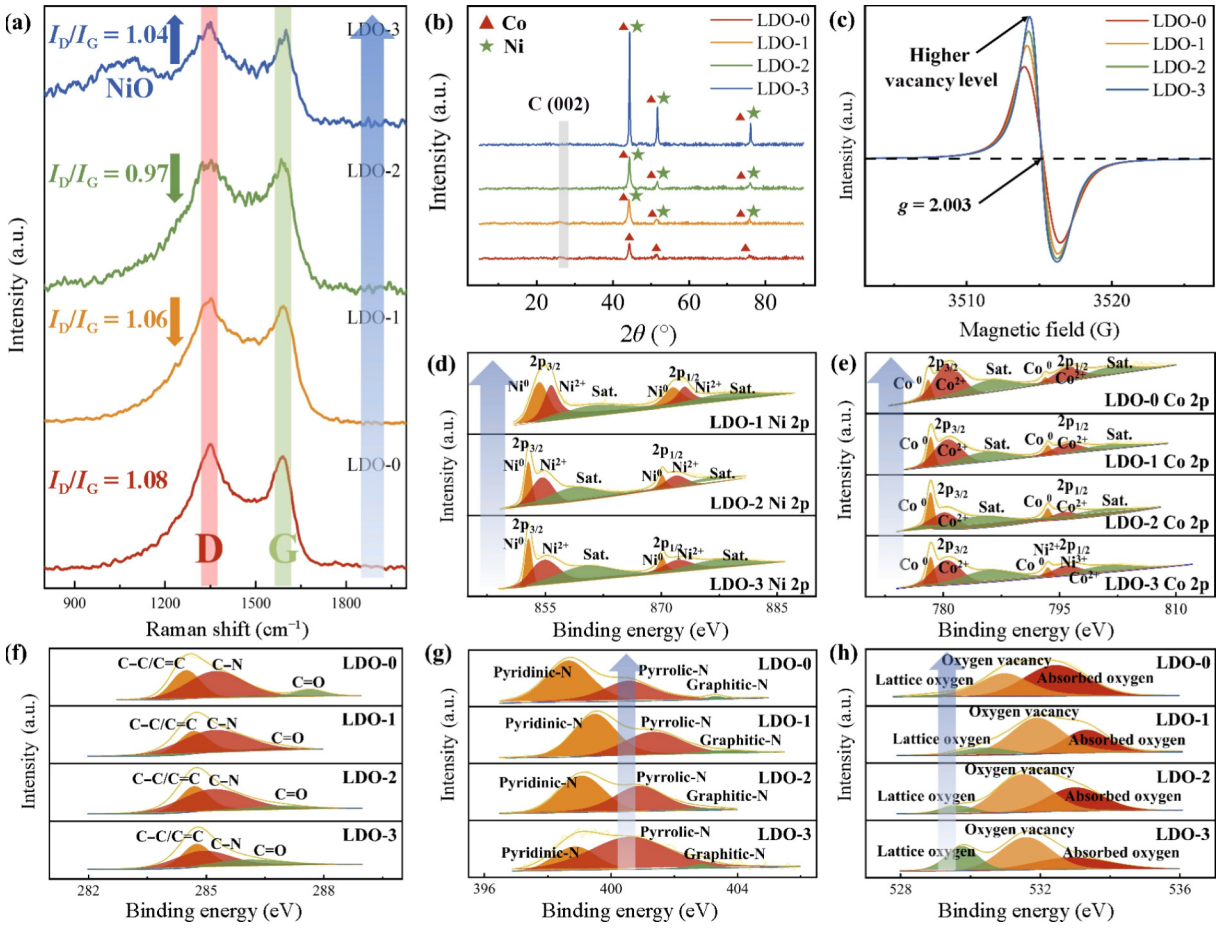

Figure 3 (a) Raman spectra, (b) XRD patterns, (c) EPR spectra, (d)–(h) XPS spectra ((d) Ni 2p peaks, (e) Co 2p peaks, (f) C 1s peaks, (g) N 1s peaks, and (h) O 1s peaks) of the samples.

concentrations of such vacancies. As the etching concentration increases, the dipole polarization loss induced by oxygen defects is progressively enhanced.

The XPS patterns of LDO are demonstrated in Figs. 3(c)–3(g). The presence of Co 2p and Ni 2p spectra proves the successful formation of CoNi alloys. Taking LDH-1 as an example, Fig. 3(c) shows the Ni 2p peaks of LDO, and the two major signaling peaks located at 853.4 and 870.7 eV are generated by spin-orbit splitting of Ni^0 2p$_{3/2}$ and Ni^0 2p$_{1/2}$ [26]. Meanwhile, the other two peaks, located at 855.8 and 873.1 eV, are generated by the spin-orbit splitting of Ni^{2+} 2p$_{3/2}$ and Ni^{2+} 2p$_{1/2}$. Figure 3(d) shows the Co 2p peaks of LDO. The prominent characteristic peaks of Co can be decomposed into three spin-orbit double peaks at 0-valent singlet Co (778.2 and 793.3 eV) as well as at +2-valent chemosynthesis state Co (780.76 and 796.26 eV), and satellite peaks (787.36 and 802.46 eV). As the etching concentration deepens, the proportion of Ni^0 increases, the proportion of Ni^{2+} decreases, and the proportion of Co^0 increases, corroborating the creation of CoNi alloys.

As observed in Fig. 3(e), the carbon in CoNi@C exists in three different forms of C–C/C=C, C–N, and C=O bonds corresponding to three peaks at 284.7, 285.9, and 288.8 eV [27]. The C–C/C=C bonding peaks are the most pronounced. As the etching concentration increases, this is very favorable for the long-range ordering of the network of carbon atoms, leading to a growth in the C–C/C=C bond peak. As a result, the abundant carbon defects introduced by both the etching and the elevated temperature carbonization process greatly enriched the polarization loss of the composites and enhance the EMW attenuation capability [28–30].

Figure 3(f) showed the N 1s split peak fitting spectrum of the LDO-1 sample. The three peaks at 398.4, 400.7, and 403.3 eV corresponded to pyridine-N, pyrrole-N, and graphite-N [31]. The content of pyrrole-N rose with the increase of the etching concentration, and the percentage of graphite N increased in LDO-1 and LDO-2 but decreased in LDO-3. As shown in Fig. 3(g), the peak energies exhibit absorbed oxygen (533 eV), oxygen vacancies (531.5 eV), and lattice oxygen (530 eV). The percentage of lattice oxygen and oxygen vacancies increases with increasing etching concentration, and the rate of absorbed oxygen decreases [32]. Generally, oxygen vacancies can behave as dipoles. The increase of oxygen vacancy occupancy enhances the dipole polarization loss [33–35].

3.3 Electromagnetic parameters and performance

The real part of the dielectric constant (ε') of the LDO all decreases with increasing frequency by the dispersion law [36, 37] in Fig. 4(a). In comparison, LDO-2 had excellent dielectric constant, meaning it had excellent EMW storage capability and electromagnetic response characteristics. As shown in Fig. 4(b), the imaginary part of the dielectric constant (ε'') also shows a similar pattern of change in ε', and LDO-2 has a more obvious advantage, indicating that the appropriate etching concentration is favorable to the dissipation of

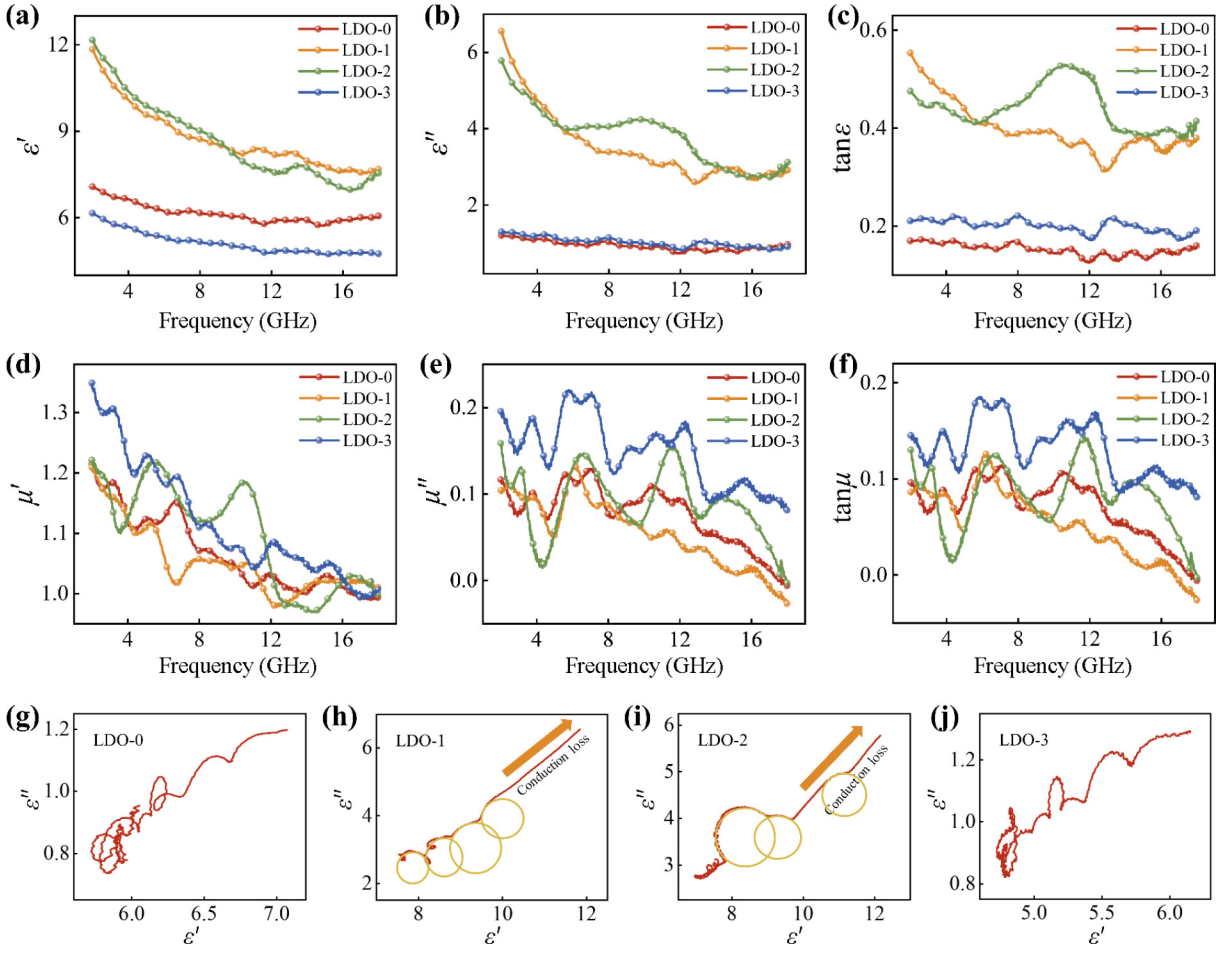

Figure 4 (a) Real part of dielectric constant, (b) imaginary part of dielectric constant, (c) dielectric loss factor, (d) real part of magnetic permeability, (e) imaginary part of magnetic permeability, (f) magnetic loss factor, and (g)–(j) Cole–Cole circle of the samples.

electromagnetic energy [38]. In Fig. 4(c), the dielectric loss angle (tanε) exhibits an increase and then a decrease with the rise of etching concentration, and LDO-2 is also higher than the other samples. Combined with the microscopic morphology analysis, after etching, the surface of the LDO all formed a rough and dense LDH worm-like structure. The difference is that LDO-1 and LDO-2 maintained a better 2D lobed skeleton structure of the precursor, creating a transparent 2D lamellar LDH layer. However, the precursor skeleton of LDO-3 was obviously damaged, and the LDH agglomeration was severe. From the dielectric aspect, the appropriate etching concentration favors forming a compact conductive network, which enhances the conduction and dielectric loss.

Based on the Debye model, the following correlation holds for ε' and ε'' of the material [39]

$$\left(\varepsilon' - \frac{(\varepsilon_s - \varepsilon_\infty)}{2}\right) + (\varepsilon'')^2 = \frac{(\varepsilon_s - \varepsilon_\infty)^2}{2} \quad (1)$$

The static and optical frequency dielectric coefficients of the material are denoted by ε_s and ε_∞. It is possible to plot the curve in terms of ε' and ε'' coordinates, which is the Cole–Cole circular curve [40]. The conductive loss capability of the material can be analyzed based on the linear tail at high frequencies. As shown in Figs. 4(g)–4(j), sample LDO-0 is dominated by polarization loss, while both LDO-1 and LDO-2 exhibit uniform linear tails, reflecting the effective enhancement of the conductive loss capability. Sample LDO-1 has four Cole–Cole circles in the low-frequency region and the straightest line tails in the high-frequency region, representing the best conductive loss capability. With further etching, the number of Cole–Cole circle decreases while the tail of the line begins to blur and zigzag. Sample LDO-3 returns to polarization loss as the primary dielectric loss mechanism, and the sharp agglomeration increases internal defects. This indicates a decrease in the conductive loss capacity due to the disruption of the structural homogeneity by the introduction of Ni. At the same time, the increase in defects promoted a rise in the contribution ratio of the polarization loss capacity.

In Figs. 4(a) and 4(b), the complex dielectric constant exhibits a decreasing trend, attributed to the phenomenon of electric dispersion. In this phenomenon, the internal polarization response lags behind the electric field changes within the material. The complex dielectric constant displays significant fluctuations in certain frequency ranges, which are often indicative of polarization relaxation phenomena occurring within the material. Furthermore, numerous heterogeneous interfaces form between CoNi and graphite. The composition and number of these interfaces influence the position and intensity of polarization peaks. In the Cole–Cole circle curves, circle approximations occur at frequencies where chirp peaks appear in the complex dielectric constant. This suggests that heterogeneous interfaces respond at these specific frequencies. These heterogeneous interfaces are associated with induced electron

aggregation and transfer, leading to the generation of internal electric fields and spatial regions. Consequently, this enhances the interfacial polarization effect. Additionally, the presence of heterogeneous interfaces causes an inhomogeneous distribution of oxygen vacancies. This promotes the development of electric fields at the heterogeneous interfaces and further facilitates charge redistribution. Moreover, differences in dielectric properties among various components lead to inhomogeneous charge distribution, resulting in spatial electric dipole moments. This, in turn, enhances polarization relaxation and converts electromagnetic waves into thermal energy.

The complex permeability of the four groups of samples is also analyzed, as shown in Figs. 4(d) and 4(e); the real (μ') and imaginary (μ'') parts of the permeability of the samples satisfy the dispersion law, and the value increases significantly with the increase of the etching concentration. The dielectric constant of the product LDO-1 after slight etching does not change much compared to that of the LDO-0 in μ'. Even the μ'' decreases in the high-frequency range instead decreases, which may be related to the ablation of the original skeleton under the initial etching condition. From Fig. 4(e), the μ'' of LDO-0 and LDO-1 inevitably had a negative value in continuously decreasing in the high-frequency region while the charge movement released too much magnetic energy [41]. When an applied magnetic field displaces the charge, an alternating electric field is induced, and sometimes, a magnetic field in the opposite direction to the applied field is induced. When the strength of the reverse magnetic field is greater than the original applied electric field, the excess magnetic energy will escape, which is expressed in the electromagnetic parameter as the negative μ''. Comparative analysis of the change rule of dielectric loss and magnetic loss angle in Figs. 4(c) and 4(f) can be found; comparing all the samples, LDO-3 has the highest loss angle ($\tan\mu$) tangent value. However, the dielectric loss effect of the samples is slightly more significant than the magnetic loss mechanism, which enhances the magnetic loss component compared to the simple ZIF-derived MAMs, and the highest value of the magnetic loss can reach near 0.2, while the highest value of the magnetic loss angle of the unmodified ZIF-L-derived absorber is only about 0.1.

The magnetization was studied by a vibrating sample magnetometer (VSM) to obtain hysteresis loops, as shown in Fig. 5(a). The four samples exhibit typical ferromagnetic behavior with obvious hysteresis loops [42]. The saturation magnetization strengths of LDO-0, LDO-1, LDO-2, and LDO-3 are 42.6, 51.3, 70.8, and 103.1 emu/g, which increase significantly with increasing Ni^{2+} etching concentration and have a significant enhancement concerning the simple ZIF-L derivative, with a substantial enhancement from the LDO-2 sample onwards, which also echoes the surge of Ni in the elemental mapping diagram. Meanwhile, the CoNi/C samples show negligible changes in coercivity (H_C) values, with H_C of 380.1, 344.9, 361.7, and 248.7 Oe for LDO-0, LDO-1, LDO-2, and LDO-3. Relatively high M_S and H_C will contribute to the high-frequency resonance, thus improving the MA performance at high frequencies [43]. To analyze the magnetic loss mechanism further, the magnetic loss is usually classified into eddy current loss, hysteresis loss, natural resonance, and exchange resonance mechanisms [44, 45].

With the further introduction of Ni elements, the magnetic permeability values of LDO-2 samples increased significantly, and LDO-3 samples possessed the highest μ' and μ''. The introduction of the LDH lamellae enhanced the weaker magnetic loss capability of the simple ZIF-derived materials, significantly strengthening the contribution of the eddy-current loss to the overall electromagnetic loss performance. From the expression of the eddy current loss factor, it can be seen that the larger the size of the particles, the stronger the intensity of the eddy current loss effect will be. Combined with the analysis of SEM (Fig. 2), it can be seen that under proper etching conditions, the sizes of LDO-1 and LDO-2 are only in the range of 5–11 μm and have relatively good dispersion and clear boundaries. When the etching concentration is too high, LDO-3 is very easy to agglomerate and increase rapidly to form dense particles with a length of more than 60 μm. When mixed with paraffin to form coaxial ring test samples, the LDO-3 samples have more substantial eddy current loss strength due to their larger particle size. Similarly, the attenuation constant α and reflection coefficient R were analyzed for the four groups of samples [12]. As shown in Fig. 5(b), the attenuation characteristics of microwave propagating in a medium are commonly expressed by the attenuation constant α. All four attenuation constant curves rise with increasing frequency. It can be found that as the etching concentration rises, the attenuation constant also rises significantly. Among them, LDO-2 has the most significant value of attenuation constant, which increases from 50 to near 203.

MA performance can be calculated from line transfer theory [46]

$$Z_{in} = Z_0\sqrt{\frac{\mu_r}{\varepsilon_r}}\tanh\left[j\frac{2\pi fd}{c}\sqrt{\varepsilon_r\mu_r}\right] \quad (2)$$

$$R_L = 20\log\left|(Z_{in}-Z_0)/(Z_{in}+Z_0)\right| \quad (3)$$

where Z_0 is the free-space impedance and Z_{in} is the normalized input impedance. d represents the thickness of the absorber. f is the test frequency. c is the velocity of the EMW. ε_r and μ_r are the complex permittivity and complex permeability.

The eddy current loss in the electromagnetic field is evaluated by the following equation [47]

$$C_0 = \mu''(\mu')^{-2}f^{-1} = 2/3\pi\mu_0 d^2\sigma \quad (4)$$

The eddy current loss factor C_0 is introduced for further analysis, as shown in Fig. 5(d). When the value of C_0 varies very little, close to the level, it represents that eddy current loss is the primary source of magnetic loss. All the samples remain constant between 8 and 18 GHz, which indicates that the eddy current effect plays a crucial role in the magnetic loss. At the same time, the natural resonance mechanism dominates in the low-frequency region. Therefore, low-frequency ferromagnetic resonance and high-frequency eddy current losses enhance the magnetic losses.

From the RL curves of LDO-0, LDO-1, LDO-2 and LDO-3 samples at different thicknesses in Figs. 5(e)–5(h), it is observed that LDO-0 has the most significant RL value of −50.6 dB at a thickness of 6.9 mm. Still, the EAB reaches 3.64 GHz only at 9.1 mm. However, after introducing the Ni element, the maximum RL and EAB were significantly enhanced, reaching −55.8 dB at 2.6 mm. In contrast, the EAB of 4.69 GHz was achieved at 2.0 mm, and the corresponding thickness was considerably thinned compared with that of LDO-0. With increasing etch concentration, the MA performance of the sample is again improved, achieving the EAB of 6.47 GHz at 2.0 mm thickness while retaining the RL value of −40.8 dB at 1.8 mm. However, due to the high etching concentration, the permeability value of LDO-3 is too high, which reduces the impedance matching, causing the EAB to drop to cover 4.79 GHz at 10 mm. In contrast, the RL value decreases significantly overall,

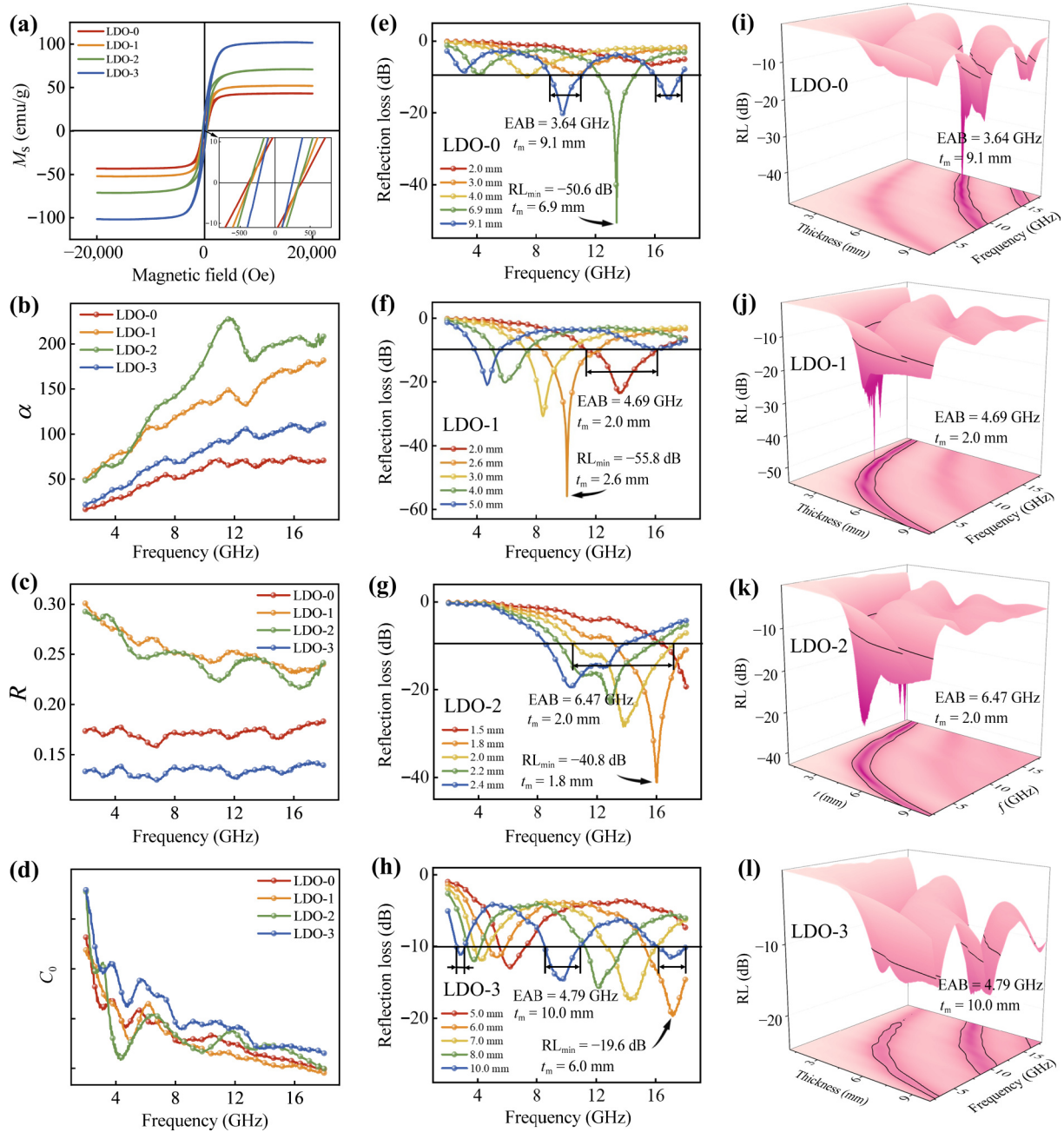

Figure 5 (a) VSM curves, (b) attenuation constant curves, (c) reflection loss curves, (d) C_0 curves, (e)–(h) EAB and RL$_{min}$, and (i)–(l) 3D reflection loss maps of the samples.

with a maximum value of only −19.6 dB at 6.0 mm, and the corresponding thickness also increases. As shown in Table S1 in the Electronic Supplementary Material (ESM), the CoNi-LDH-derived material in this paper has apparent advantages in terms of lightweight and EMA properties compared to some reported 2D materials.

Table 1 and Fig. 6 compare the MA performance of this work with some MOFs derivatives in recent years. It can be seen that the MOFs derivative material obtained in this work achieves extremely impressive MA properties with low mass ratio and low thickness, which has the outstanding advantages of light weight and high efficiency.

As a result of the above discussions, the MA mechanism of CoNi@C-LDO is systematically summarized in Fig. 7. First, the hollow structure and complex surface induced by ion etching provide more propagation paths, thus attenuating the microwave by multiple reflections and scattering [58]. Moreover, the hollow structure and complex surface significantly increase the specific surface area of the material, providing more attachment sites and enhancing the trapping of free electrons [59]. Second, the CoNi-graphite non-homogeneous interface with noticeable electronegativity difference is formed on the surface, which quickly attracts charges and induces charge penetration and migration, significantly enhancing the interfacial polarization loss of electromagnetic energy [60]. Third, the presence of metal elements would dramatically facilitate the graphitization of the carbon atoms around them. So, it was likely to be insufficiently graphitized or even formed defects where the distribution of metal elements was

Table 1 Comparison of this work with some recently reported MA properties of MOFs materials

Samples	Mass ratio	Thickness (mm)	RL (dB)	EAB (GHz)	Ref.
Fe_3O_4/C	50%	1.8	−42	5.1	[48]
Fe/C	30%	4.0	−40.42	4.34	[49]
NiFe@NC	30%	1.75	−60.48	5.12	[50]
Co/MoC@NC	20%	1.85	−68.68	4.45	[51]
CoFe/C	40%	2.15	−44.6	5.5	[52]
C/Co	50%	2.0	−51.6	4.32	[53]
YS-NiFe/GC@C	60%	3.5	−56.3	5.64	[54]
DMM-700	55%	2.4	−56.4	4	[55]
Co/C-HS-600	30%	2.0	−31.3	4.4	[56]
Ni-C-ZnO	25%	2.5	−55.8	4.1	[57]
CoNi@C-LDO	30%	2.0	−40.8	6.47	This work

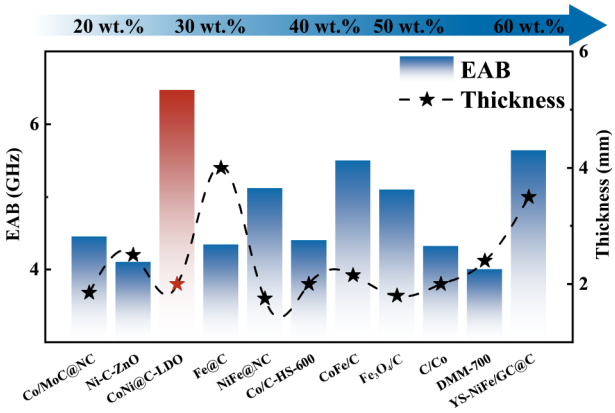

Figure 6 Comparison of this work with some recently reported MA properties of MOFs materials.

not adequate [61]. Many charges would accumulate, rotate, and collide at the boundaries of the defects, which enhanced the defect-induced polarization process and thus increased the loss of electromagnetic energy into thermal energy. Fourth, the etching and growth process of Ni^{2+} sheared off quantities of organic matter and introduced extra oxygen atoms. This significantly increases carbon-oxygen functional groups, promoting the dipole polarization process in dielectric losses [62]. Fifthly, the magnetic CoNi nanoparticles were uniformly embedded in graphitic carbon nanonetworks, which gave rise to complex magnetic resonance and eddy current losses [63]. Finally, the void structure and the appropriate magnetic/carbon ratio optimize the impedance matching and electromagnetic attenuation. All in all, the hollow structure, complex surface as well as electromagnetic component optimization due to ion etching all significantly enhance the dielectric and magnetic losses of the MA process.

4 Conclusion

In this work, we have used a particular 2D material, ZIF-L, as a template to construct a series of CoNi-LDH materials with different morphologies and structures and have comparatively analyzed the MA properties of the derivative LDO materials of the resulting products. The complete conversion of ZIF-L to CoNi-LDH was achieved by regulating the appropriate etching concentration while avoiding the complete collapse of the 2D lamellar skeleton and the severe accumulation of the LDH nanosheets caused by excessive etching. The hollow structures and complex surfaces induced by ion etching provide a larger specific surface area, resulting in more attachment sites and broader propagation paths. This facilitates the active site exposure and electron transport, as well as attenuating EMW through multiple reflections and scattering. At the same time, the etching process forms many defects, polar functional groups, and apparent non-homogeneous structures, which greatly enhance the polarization loss and conductivity loss of the wave-absorbing process, thus strengthening the dielectric loss. In addition, introducing the magnetic component Ni element optimizes the electromagnetic component and improves the impedance matching of the material, enhancing the magnetic loss. In conclusion, the induced conversion of MOFs to LDH improves the impedance matching and enhances multiple loss mechanisms, thus increasing the MA level. The resulting LDH-derived product, LDO-2, has the best MA performance, which can achieve the EAB of 6.47 GHz at a thickness of 2.0 mm while retaining the maximum RL value of −40.8 dB at 1.8 mm. Compared to the precursor derivatives, the broadband absorption performance was improved by 78%. The prepared 2D CoNi-LDH-derived materials possess skinny thickness and a specific surface area, exhibit better wave absorption properties than the precursors, and have great potential for MA applications.

Electronic Supplementary Material: Supplementary material (characterization detail, BET surface area maps, nitrogen adsorption–desorption isotherm maps, pore size distributions maps, and comparison of MA properties with reported 2D materials) is available in the online version of this article at https://doi.org/10.26599/NR.2025.94907283.

Data availability

All data needed to support the conclusions in the paper are presented in the manuscript and the Electronic Supplementary Material. Additional data related to this paper may be requested from the corresponding author upon request.

Acknowledgements

This work is supported by the National Natural Science Foundation of China (No. 52172295), Young talent lift project (No. 2021-JCJQ-QT-064), the Postgraduate Research & Practice Innovation Program of Jiangsu Province (No. KYCX24_0571), and the

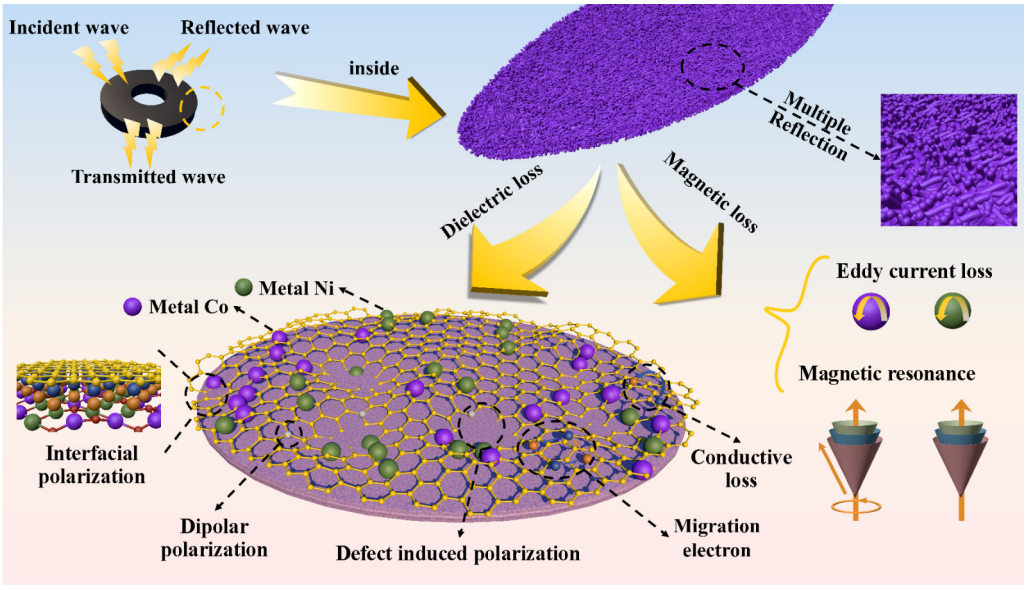

Figure 7 Microwave absorption mechanism diagram.

Postgraduate Research & Practice Innovation Program of Jiangsu Province (No. KYCX23_0371).

Declaration of competing interest

All the contributing authors report no conflict of interests in this work.

Author contribution statement

Z. L. N.: Experimental design, performed experiments, data curation, validation, writing manuscript. H. X. H.: Project administration, funding acquisition. Y. R. H.: Experimental design, performed experiments, data curation. Y. J. L.: Data curation, validation.J. Q. T.: Data curation, validation. L. T. D.: Data curation. Y. C. W.: Data curation. Z. Y. C.: Validation. Z. L. L.: Validation. J. T. Z.: Project administration, funding acquisition. All the authors have approved the final manuscript.

Use of AI statement

None.

References

[1] Lv, H. L.; Yang, Z. H.; Pan, H. G.; Wu, R. B. Electromagnetic absorption materials: Current progress and new frontiers. *Prog. Mater. Sci.* **2022**, *127*, 100946.

[2] Liu, Y. J.; Zhou, J. T.; Ning, Z. L.; Huang, H. X.; Cheng, Z. Y.; Duan, L. T.; Wang, Y. C.; Tao, X. W.; Liu, P. J.; Ma, Y. et al. Multi-interfacial heterostructure design of carbon fiber/silicone rubber-oriented composites for microwave absorption and thermal management. *Adv. Funct. Mater.* **2024**, *34*, 2411573.

[3] Chen, G.; Li, Z. J.; Zhang, L. M.; Chang, Q.; Chen, X. J.; Fan, X. M.; Chen, Q.; Wu, H. J. Mechanisms, design, and fabrication strategies for emerging electromagnetic wave-absorbing materials. *Cell Rep. Phys. Sci.* **2024**, *5*, 102097.

[4] Liu, Y. J.; Zhou, J. T.; Li, C. C.; Zhang, H. H.; Wang, Y. C.; Yan, Y.; Duan, L.; Cheng, Z. Y.; Ma, Y.; Yao, Z. J. Interfacial coupling effects in two-dimensional ordered arrays for microwave attenuation. *Nat. Commun.* **2025**, *16*, 202.

[5] Huang, M. Q.; Wang, L.; Pei, K.; You, W. B.; Yu, X. F.; Wu, Z. C.; Che, R. C. Multidimension-controllable synthesis of MOF-derived Co@N-doped carbon composite with magnetic–dielectric synergy toward strong microwave absorption. *Small* **2020**, *16*, 2000158.

[6] Tao, J. Q.; Xu, L. L.; Jin, H. S.; Gu, Y. S.; Zhou, J. T.; Yao, Z. J.; Tao, X. W.; Chen, P.; Wang, D. W.; Li, Z. et al. Selective coding dielectric genes based on proton tailoring to improve microwave absorption of MOFs. *Adv. Powder Mater.* **2023**, *2*, 100091.

[7] Wu, Z. C.; Cheng, H. W.; Jin, C.; Yang, B. T.; Xu, C. Y.; Pei, K.; Zhang, H. B.; Yang, Z. Q.; Che, R. C. Dimensional design and core–shell engineering of nanomaterials for electromagnetic wave absorption. *Adv. Mater.* **2022**, *34*, 2107538.

[8] Tao, J. Q.; Zou, K. X.; Zhou, J. T.; Wu, H. J.; Xu, L. L.; Wang, J.; Tao, X. W.; Huang, H. X.; Yao, Z. J. Phenolic multiple kinetics-dynamics and discrete crystallization thermodynamics in amorphous carbon nanostructures for electromagnetic wave absorption. *Nat. Commun.* **2024**, *15*, 10337.

[9] Guo, Z. Q.; Lan, D.; Jia, Z. R.; Gao, Z. G.; Shi, X. T.; He, M. K.; Guo, H.; Wu, G. L.; Yin, P. F. Multiple tin compounds modified carbon fibers to construct heterogeneous interfaces for corrosion prevention and electromagnetic wave absorption. *Nano-Micro Lett.* **2025**, *17*, 23.

[10] Zhao, T. B.; Lan, D.; Jia, Z. R.; Gao, Z. G.; Wu, G. L. Hierarchical porous molybdenum carbide synergic morphological engineering towards broad multi-band tunable microwave absorption. *Nano Res.* **2024**, *17*, 9845–9856.

[11] Tao, J. Q.; Tan, R. Y.; Xu, L. L.; Zhou, J. T.; Yao, Z. J.; Lei, Y. M.; Chen, P.; Li, Z.; Ou, J. Z. Ion-exchange strategy for metal-organic frameworks-derived composites with tunable hollow porous and microwave absorption. *Small Methods* **2022**, *6*, e2200429.

[12] Zhang, X. F.; Wang, Z. Y.; Xu, L. L.; Zuraiqi, K.; Daeneke, T.; Yao, Z. J.; Qi, D. C.; Zavabeti, A. Liquid metal derived MOF functionalized nanoarrays with ultra-wideband electromagnetic absorption. *J. Colloid Interface Sci.* **2022**, *606*, 1852–1865.

[13] Hui, S. C.; Zhou, X.; Zhang, L. M.; Wu, H. J. Constructing multiphase-induced interfacial polarization to surpass defect-induced polarization in multielement sulfide absorbers. *Adv. Sci.* **2024**, *11*, 2307649.

[14] Jia, Z. R.; Sun, L. F.; Gao, Z. G.; Lan, D. Modulating magnetic interface layer on porous carbon heterostructures for efficient microwave absorption. *Nano Res.* **2024**, *17*, 10099–10108.

[15] Chen, G.; Liang, H. S.; Yun, J. J.; Zhang, L. M.; Wu, H. J.; Wang, J. Y. Ultrasonic field induces better crystallinity and abundant defects at

grain boundaries to develop CuS electromagnetic wave absorber. *Adv. Mater.* **2023**, *35*, 2305586.
[16] Jin, J.; Yue, X. Y.; Pan, D.; Guo, Y.; Liu, C. T.; Shen, C. Y.; Liu, H. Glucose derived carbon encapsulated boron nitride core–shell composites for efficient electromagnetic microwave absorption. *Compos. Commun.* **2024**, *48*, 101942.
[17] Liu, Z. K.; Chen, J.; Que, M. D.; Zheng, H. Q.; Yang, L. F.; Yuan, H. D.; Ma, Y. Z.; Li, Y. J.; Yang, X. F. 2D $Ti_3C_2T_x$ MXene/MOFs composites derived CoNi bimetallic nanoparticles for enhanced microwave absorption. *Chem. Eng. J.* **2022**, *450*, 138442.
[18] Yang, H. L.; Li, C. Q.; Mo, R. W.; Wang, J. N. Facile preparation and broadband microwave absorption of multilayered materials based on thin films of reduced graphene oxide. *Carbon* **2024**, *224*, 119093.
[19] He, Y. R.; Zhou, J. T.; Tao, J. Q.; Zhang, X. J.; Yao, Z. J.; Hao, X. Q. A control strategy for microwave absorption performance on a two-dimensional scale. *Chem. Eng. J.* **2023**, *472*, 144841.
[20] Yuan, H. Y.; Aljneibi, S. A. A. A.; Yuan, J. R.; Wang, Y. X.; Liu, H.; Fang, J.; Tang, C. H.; Yan, X. H.; Cai, H.; Gu, Y. D. et al. ZnO nanosheets abundant in oxygen vacancies derived from metal-organic frameworks for ppb-level gas sensing. *Adv. Mater.* **2019**, *31*, 1807161.
[21] Tao, K.; Han, X.; Ma, Q. X.; Han, L. A metal-organic framework derived hierarchical nickel-cobalt sulfide nanosheet array on Ni foam with enhanced electrochemical performance for supercapacitors. *Dalton Trans.* **2018**, *47*, 3496–3502.
[22] Lü, Y. Y.; Wang, Y. T.; Li, H. L.; Lin, Y.; Jiang, Z. Y.; Xie, Z. X.; Kuang, Q.; Zheng, L. S. MOF-derived porous Co/C nanocomposites with excellent electromagnetic wave absorption properties. *ACS Appl. Mater. Interfaces* **2015**, *7*, 13604–13611.
[23] ur Rehman, S.; Wang, J. M.; Luo, Q. H.; Sun, M. Z.; Jiang, L.; Han, Q.; Liu, J. C.; Bi, H. Starfish-like C/$CoNiO_2$ heterostructure derived from ZIF-67 with tunable microwave absorption properties. *Chem. Eng. J.* **2019**, *373*, 122–130.
[24] Liang, L. L.; Liu, Z.; Xie, L. J.; Chen, J. P.; Jia, H.; Kong, Q. Q.; Sun, G. H.; Chen, C. M. Bamboo-like N-doped carbon tubes encapsulated CoNi nanospheres towards efficient and anticorrosive microwave absorbents. *Carbon* **2021**, *171*, 142–153.
[25] Liu, G.; Tu, J. Q.; Wu, C.; Fu, Y. J.; Chu, C. H.; Zhu, Z. H.; Wang, X. H.; Yan, M. High-yield two-dimensional metal-organic framework derivatives for wideband electromagnetic wave absorption. *ACS Appl. Mater. Interfaces* **2021**, *13*, 20459–20466.
[26] Zhao, B.; Li, Y.; Ji, H. Y.; Bai, P. W.; Wang, S.; Fan, B. B.; Guo, X. Q.; Zhang, R. Lightweight graphene aerogels by decoration of 1D CoNi chains and CNTs to achieve ultra-wide microwave absorption. *Carbon* **2021**, *176*, 411–420.
[27] Li, Z. J.; Lin, H.; Ding, S. Q.; Ling, H. L.; Wang, T.; Miao, Z. Q.; Zhang, M.; Meng, A. L.; Li, Q. D. Synthesis and enhanced electromagnetic wave absorption performances of Fe_3O_4@C decorated walnut shell-derived porous carbon. *Carbon* **2020**, *167*, 148–159.
[28] Sun, C. H.; Lan, D.; Jia, Z. R.; Gao, Z. G.; Wu, G. L. Kirkendall effect-induced ternary heterointerfaces engineering for high polarization loss MOF-LDH-MXene absorbers. *Small* **2024**, *20*, 2405874.
[29] Liu, Y.; Ren, X. Y.; Zhou, X. F.; Lan, D.; Gao, Z. G.; Jia, Z. R.; Wu, G. L. Defect design and vacancy engineering of $NiCo_2Se_4$ spinel composite for excellent electromagnetic wave absorption. *Ceram. Int.* **2024**, *50*, 46643–46652.
[30] Zhu, J. H.; Lan, D.; Liu, X. H.; Zhang, S. H.; Jia, Z. R.; Wu, G. L. Porous structure fibers based on multi-element heterogeneous components for optimized electromagnetic wave absorption and self-anticorrosion performance. *Small* **2024**, *20*, 2403689.
[31] Chen, F.; Luo, H.; Cheng, Y. Z.; Guo, R. D.; Yang, W. T.; Wang, X.; Gong, R. Z. Nickel/Nickel phosphide composite embedded in N-doped carbon with tunable electromagnetic properties toward high-efficiency microwave absorption. *Compos. Part A: Appl. Sci. Manu.* **2021**, *140*, 106141.
[32] Shu, J. C.; Huang, X. Y.; Cao, M. S. Assembling 3D flower-like Co_3O_4-MWCNT architecture for optimizing low-frequency microwave absorption. *Carbon* **2021**, *174*, 638–646.
[33] Zhang, Y.; Lan, D.; Hou, T. Q.; Jia, M. S.; Jia, Z. R.; Gu, J. W.; Wu, G. L. Multifunctional electromagnetic wave absorbing carbon fiber/$Ti_3C_2T_x$ MXene fabric with ultra-wide absorption band. *Carbon* **2024**, *230*, 119594.
[34] Cheng, Y. H.; Lan, D.; Jia, Z. R.; Gao, Z. G.; Liu, X. H.; Shi, X. T.; He, M. K.; Guo, H.; Wu, G. L. MOF derivatives anchored to multichannel hollow carbon fibers with gradient structures for corrosion resistance and efficient electromagnetic wave absorption. *J. Mater. Sci. Technol.* **2025**, *216*, 150–164.
[35] Han, M. J.; Lan, D.; Zhang, Z. M.; Zhao, Y. Z.; Zou, J. X.; Gao, Z. G.; Wu, G.L.; Jia, Z. R. Micro-sized hexapod-like CuS/Cu_9S_5 hybrid with broadband electromagnetic wave absorption. *J. Mater. Sci. Technol.* **2025**, *214*, 302–312.
[36] Gu, W. H.; Sheng, J. Q.; Huang, Q. Q.; Wang, G. H.; Chen, J. B.; Ji, G. B. Environmentally friendly and multifunctional shaddock peel-based carbon aerogel for thermal-insulation and microwave absorption. *Nano-Micro Lett.* **2021**, *13*, 102.
[37] Li, Y.; Meng, F. B.; Mei, Y.; Wang, H. G.; Guo, Y. F.; Wang, Y.; Peng, F. X.; Huang, F.; Zhou, Z. W. Electrospun generation of $Ti_3C_2T_x$ MXene@graphene oxide hybrid aerogel microspheres for tunable high-performance microwave absorption. *Chem. Eng. J.* **2020**, *391*, 123512.
[38] Cheng, R. R.; Wang, Y.; Di, X. C.; Lu, Z.; Wang, P.; Ma, M. L.; Ye, J. R. Construction of MOF-derived plum-like NiCo@C composite with enhanced multi-polarization for high-efficiency microwave absorption. *J. Colloid Interface Sci.* **2022**, *609*, 224–234.
[39] Lei, L.; Yao, Z. J.; Zhou, J. T.; Zheng, W. J.; Wei, B.; Zu, J. Q.; Yan, K. Y. Hydrangea-like Ni/NiO/C composites derived from metal-organic frameworks with superior microwave absorption. *Carbon* **2021**, *173*, 69–79.
[40] Liu, P. B.; Huang, Y.; Yan, J.; Yang, Y. W.; Zhao, Y. Construction of CuS nanoflakes vertically aligned on magnetically decorated graphene and their enhanced microwave absorption properties. *ACS Appl. Mater. Interfaces* **2016**, *8*, 5536–5546.
[41] Wang, Z. C.; Wei, R. B.; Gu, J. W.; Liu, H.; Liu, C. T.; Luo, C. J.; Kong, J.; Shao, Q.; Wang, N.; Guo, Z. H. et al. Ultralight, highly compressible and fire-retardant graphene aerogel with self-adjustable electromagnetic wave absorption. *Carbon* **2018**, *139*, 1126–1135.
[42] Huang, M. Q.; Wang, L.; You, W. B.; Che, R. C. Single zinc atoms anchored on MOF-derived N-doped carbon shell cooperated with magnetic core as an ultrawideband microwave absorber. *Small* **2021**, *17*, 2101416.
[43] Zhu, X. Y.; Qiu, H. F.; Chen, P.; Chen, G. Z.; Min, W. X. Anemone-shaped ZIF-67@CNTs as effective electromagnetic absorbent covered the whole X-band. *Carbon* **2021**, *173*, 1–10.
[44] Quan, B.; Liang, X. H.; Ji, G. B.; Ma, J. N.; Ouyang, P. Y.; Gong, H.; Xu, G. Y.; Du, Y. W. Strong electromagnetic wave response derived from the construction of dielectric/magnetic media heterostructure and multiple interfaces. *ACS Appl. Mater. Interfaces* **2017**, *9*, 9964–9974.
[45] Wang, Y.; Di, X. C.; Lu, Z.; Cheng, R. R.; Wu, X. M.; Gao, P. H. Controllable heterogeneous interfaces of cobalt/carbon nanosheets/rGO composite derived from metal-organic frameworks for high-efficiency microwave attenuation. *Carbon* **2022**, *187*, 404–414.
[46] Wang, Y.; Gao, X.; Wu, X. M.; Zhang, W. Z.; Luo, C. Y.; Liu, P. B. Facile design of 3D hierarchical $NiFe_2O_4$/N-GN/ZnO composite as a high performance electromagnetic wave absorber. *Chem. Eng. J.* **2019**, *375*, 121942.

[47] Wei, B.; Zhou, J. T.; Yao, Z. J.; Haidry, A. A.; Qian, K.; Lin, H. Y.; Guo, X. L.; Chen, W. J. Excellent microwave absorption property of nano-Ni coated hollow silicon carbide core–shell spheres. *Appl. Surf. Sci.* **2020**, *508*, 145261.

[48] Kavoosi, V.; Masoudpanah, S. M. PVP-assisted MOF-derived Fe_3O_4/C powders for microwave absorption applications. *Heliyon* **2025**, *11*, e41202.

[49] Xu, X.; Li, X. M.; Yang, H. Z.; Zhang, G. S.; Xia, L.; Wen, G. W.; Wang, D.; Huang, X. X.; Zhang, R. Application of carbon-based MOF derived Fe/C composites toward excellent microwave absorption. *Mater. Sci. Eng.: B* **2025**, *312*, 117786.

[50] Li, Z. T.; Chen, J.; Ma, Y. Z.; Li, Y. J.; Yang, X. F. MXene/bimetallic NiFe-MOF derived magnetic-dielectric synergistic composites with the charge transfer of multiple heterogeneous interfaces for excellent microwave absorption. *J. Alloy. Compd.* **2025**, *1010*, 177955.

[51] Guo, Y. M.; Zhu, Y. W.; Sun, J.; Lin, Y. X.; Li, X. Y.; Liu, G.; Gong, Y.; Zhang, X.; Tian, X. Y.; Li, X. X. et al. MOF-derived carbon nanotube bridged Co/MoC@NC composites for enhanced electromagnetic wave absorption. *J. Alloy. Compd.* **2025**, *1010*, 177346.

[52] Liang, X. H.; Wang, G. H.; Gu, W. H.; Ji, G. B. Prussian blue analogue derived carbon-based composites toward lightweight microwave absorption. *Carbon* **2021**, *177*, 97–106.

[53] Wang, M. Q.; Shu, J. C.; Wan, X.; Cao, W. Q.; Cao, M. S. Thermally derived hierarchical nanoplates for electromagnetic protection and waste energy recovery device. *Small* **2023**, *19*, 2303186.

[54] Tang, C. H.; Ma, W. J.; He, P.; Zhou, Y. K.; Liu, X. Y.; Zuo, P. Y.; Zhuang, Q. X. Encapsulated prussian blue analogs derived nanocubes with tunable yolk–shell structure enabling highly efficient microwave absorption. *Carbon* **2023**, *215*, 118462.

[55] Wu, F.; Wan, L. Y.; Li, Q. Y.; Zhang, Q. Y.; Zhang, B. L. Ternary assembled MOF-derived composite: Anisotropic epitaxial growth and microwave absorption. *Compos. B: Eng.* **2022**, *236*, 109839.

[56] Li, Z. N.; Han, X. J.; Ma, Y.; Liu, D. W.; Wang, Y. H.; Xu, P.; Li, C. L.; Du, Y. C. MOFs-derived hollow Co/C microspheres with enhanced microwave absorption performance. *ACS Sustainable Chem. Eng.* **2018**, *6*, 8904–8913.

[57] Wang, L.; Yu, X. F.; Li, X.; Zhang, J.; Wang, M.; Che, R. C. MOF-derived yolk-shell Ni@C@ZnO Schottky contact structure for enhanced microwave absorption. *Chem. Eng. J.* **2020**, *383*, 123099.

[58] Mu, C. P.; Du, X.; Nie, A. M.; Wang, B. C.; Wen, F. S.; Xiang, J. Y.; Zhai, K.; Liu, Z. Y. Microwave absorption properties of heterostructure composites of two dimensional layered magnetic materials and graphene nanosheets. *Appl. Phys. Lett.* **2019**, *115*, 043103.

[59] Tan, R. Y.; Zhou, J. T.; Yao, Z. J.; Wei, B.; Zu, J. Q.; Lin, H. Y.; Li, Z. Ferrero Rocher® chocolates-like FeCo/C microspheres with adjustable electromagnetic properties for effective microwave absorption. *J. Alloy. Compd.* **2021**, *857*, 157568.

[60] Xu, C. Y.; Wang, L.; Li, X.; Qian, X.; Wu, Z. C.; You, W. B.; Pei, K.; Qin, G.; Zeng, Q. W.; Yang, Z. Q. et al. Hierarchical magnetic network constructed by CoFe nanoparticles suspended within "tubes on rods" matrix toward enhanced microwave absorption. *Nano-Micro Lett.* **2021**, *13*, 47.

[61] Yang, L. J.; Deng, T. W.; Jia, Z. R.; Zhou, X. D.; Lv, H. L.; Zhu, Y. T.; Liu, J. C.; Yang, Z. H. Hierarchical porous hollow graphitized carbon@MoS_2 with wideband EM dissipation capability. *J. Mater. Sci. Technol.* **2021**, *83*, 239–247.

[62] Wei, B.; Zhou, C. Y.; Yao, Z. J.; Chen, P.; Wang, M. Q.; Li, Z. J.; Zhou, J. T.; Hou, J. S.; Li, W. Encapsulation of high specific surface area red blood cell-like mesoporous carbon spheres by magnetic nanoparticles: A new strategy to realize multiple electromagnetic wave loss mechanism. *Carbon* **2021**, *184*, 232–244.

[63] Wang, B. C.; Ji, Y.; Mu, C. P.; Huo, Y. J.; Xiang, J. Y.; Nie, A. M.; Xue, T. Y.; Zhai, K.; Liu, Z. Y.; Wen, F. S. Well-controlled Core-shell structures based on Fe_3O_4 nanospheres coated by polyaniline for highly efficient microwave absorption. *Appl. Surf. Sci.* **2022**, *591*, 153176.